

Longitudinal Kerr effect in ultrathin Fe films on Pd(100)

A. Vernes, I. Reichl, and P. Weinberger

Center for Computational Materials Science, Technical University Vienna, Gumpendorferstrasse 1a, A-1060 Vienna, Austria

L. Szunyogh

*Center for Computational Materials Science, Technical University Vienna, Gumpendorferstrasse 1a, A-1060 Vienna, Austria
and Department of Theoretical Physics, University of Technology and Economics, Budafoki út 8, H-1521 Budapest, Hungary*

C. Sommers

Laboratoire de Physique des Solides, Université de Paris-Sud, F-91405 Orsay, France

(Received 4 June 2004; published 10 November 2004)

Based on Luttinger's formulation the complex optical conductivity tensor of ultrathin films of Fe on Pd(100) is calculated by means of the spin-polarized relativistic screened Korringa-Kohn-Rostoker method using a contour integration technique. For longitudinal geometry and oblique incidence *ab initio* Kerr spectra are then obtained via a 2×2 matrix technique that takes into account all multiple reflections between layers and optical interferences. The obtained results are in very good agreement with the available experimental data.

DOI: 10.1103/PhysRevB.70.195407

PACS number(s): 78.20.Ls, 71.15.Rf, 78.66.Bz, 78.67.Pt

I. INTRODUCTION

The interest in the dependence of magnetic properties in case of Fe/Pd(100) layered systems on the film morphology dates back more than ten years.^{1,2} Presently the following peculiarities concerning the properties of Fe ultrathin films on Pd(100) are known from the literature: (1) different deposition methods, i.e., thermal or pulse laser deposition, and temperatures provide different magnetizations^{2,3} and (2) there is a reorientation of the magnetization from out of plane to in plane around a critical thickness of about 2.5 monolayers (ML) of Fe,¹ which is well reproduced by *ab initio* calculations.⁴ Furthermore, independent of an in- or out-of-plane direction of the magnetization, the Curie temperature increases monotonically with the Fe thickness.¹ Caused by the lattice constant misfit between bcc Fe and fcc Pd, two different growth modes are experimentally predicted for Fe/Pd(100)—namely, a layer-by-layer one^{5,6} and another one in which two-dimensional islands of Fe are formed on top of the Pd substrate.⁷

In the present contribution the longitudinal magneto-optical Kerr effect (LMOKE) and magnetic properties of Fe/Pd(100) are investigated using a first-principles approach with the Fe thicknesses ranging from the submonolayer regime up to ten atomic layers as based on experimentally determined profiles.^{3,8}

II. OPTICAL CONDUCTIVITY TENSOR

In terms of the current-current correlation function⁹

$$\tilde{\Sigma}_{\mu\nu}(\omega) = \frac{i\hbar}{V} \sum_{m,n} \frac{f(\varepsilon_m) - f(\varepsilon_n)}{\varepsilon_m - \varepsilon_n + \hbar\omega + i\delta} J_{mn}^\mu J_{nm}^\nu, \quad (1)$$

with $f(\varepsilon)$ being the Fermi-Dirac distribution function, ε_m and ε_n a pair of eigenvalues of the one-electron Hamiltonian, J_{mn}^μ matrix elements of the electronic current operator ($\mu=x,y,z$), and V the reference (crystalline) volume, the

complex optical conductivity $\tilde{\sigma}_{\mu\nu}(\omega)$ is given by the well-known Luttinger formula¹⁰

$$\tilde{\sigma}_{\mu\nu}(\omega) = \frac{\tilde{\Sigma}_{\mu\nu}(\omega) - \tilde{\Sigma}_{\mu\nu}(0)}{\hbar\omega + i\delta}. \quad (2)$$

In contrast to the widely used Wang-Callaway formula for the optical conductivity,¹¹ the Luttinger formula (2) has the advantage that it simultaneously provides the absorptive and the dispersive parts on the same footing without using the Kramers-Krönig relations.⁹ The current-current correlation function $\tilde{\Sigma}_{\mu\nu}(\omega)$ in Eq. (1) is evaluated by performing contour integrations.¹² From a numerical point of view, aside from the Matsubara poles, $\tilde{\Sigma}_{\mu\nu}(\omega)$ depends on the number of complex energy points n_z considered for the energy integrals and on the number of \vec{k} points used to calculate the scattering path operator within the spin-polarized relativistic screened Korringa-Kohn-Rostoker (SKKR) method and $\tilde{\Sigma}_{\mu\nu}(z \pm \hbar\omega + i\delta, z)$ for a given energy z , respectively. For this reason two efficient schemes have been introduced to control the accuracy of the z and \vec{k} integrations.¹³

III. LMOKE FOR OBLIQUE INCIDENCE

In a previous paper,¹⁴ it was shown in detail that for polar geometry and normal incidence the 2×2 matrix technique takes into account all possible reflections and optical interferences within a layered system. Therefore, in here only those aspects of the 2×2 matrix technique are briefly summarized which are needed for describing the Kerr effect for oblique incidence in a longitudinal geometry—i.e., when the magnetization is in the plane of incidence and perpendicular to the surface normal.

A. Basic concepts

Consider a right-handed Cartesian coordinate system with the origin at the interface, the z axis being parallel to the

surface normal and pointing into the vacuum. If the 0yz plane is chosen as the plane of incidence, longitudinal geometry implies that the magnetization \vec{M}_p is oriented in each layer p parallel to the y axis. The numbering of layers is assumed to start at the first layer on top of the semi-infinite substrate ($p=1$) such that if the system consists of N layers, the surface layer is labeled by $p=N$. Furthermore, it is convenient to introduce the index $p=0$ for the substrate and $p=N+1$ for the vacuum. The lower and upper boundaries of a particular layer p are planes at z_p and z_{p+1} with $z_p < z_{p+1}$. The interface to the vacuum is a plane at $z_{N+1}=0$, whereas the lower boundary of the substrate is at $z_0=-\infty$. From an optical point of view each layer and therefore also the substrate are assumed to be a homogeneous, linear, and anisotropic conducting medium.

The harmonic plane wave for a complex electric (magnetic) field is of the form

$$\vec{E}_p(\vec{r}, t) = \vec{E}_p \exp[i(\vec{q}_p \vec{r} - \omega t)] \exp(-\delta t) = \vec{E}_p \exp[i(\vec{q}_p \vec{r} - \tilde{\omega} t)], \quad (3)$$

where \vec{q}_p is the complex propagation vector and $\tilde{\omega} = \omega - i\delta$ the complex frequency.¹⁵ In terms of the spherical colatitude θ ($0 \leq \theta < \pi/2$) and longitude φ ($0 \leq \varphi \leq 2\pi$) of the incident beam, for a longitudinal geometry and oblique incidence (θ arbitrary and $\varphi = \pi/2$) the propagation vector \vec{q}_p is given by

$$\vec{q}_p = q_0 \vec{n}_p = q_0 (-\sin \theta \vec{e}_y + \tilde{n}_p \cos \theta \vec{e}_z), \quad (4)$$

where \vec{n}_p is the complex refractive vector in layer p ,

$$\begin{cases} \tilde{n}_{px} = 0, \\ \tilde{n}_{py} = -\sin \theta, \\ \tilde{n}_{pz} = \tilde{n}_p \cos \theta, \end{cases} \quad (5)$$

q_0 the propagation constant in vacuum, and $\vec{e}_x, \vec{e}_y, \vec{e}_z$ are the unit vectors along the coordinate axes. Here the Cartesian components of \vec{n}_p are given by using the continuity of the electric and magnetic fields at the boundary between adjacent layers and the interface,¹⁶ which implies that the x and y components of the wave vector are the same on both sides of a boundary—namely, $\tilde{n}_{p\mu} = \tilde{n}_{N+1, \mu} \equiv \tilde{n}_\mu$ for $\mu = x, y$ and $\forall p = 1, \dots, N+1$. According to the complex propagation vector in Eq. (4), Eq. (3) can be written as

$$\begin{aligned} \vec{E}_p(\vec{r}, t) &= \vec{\mathcal{E}}_p \exp[i(q_0 \tilde{n}_{pz} z - \tilde{\omega} t)], \\ &\text{with } \vec{\mathcal{E}}_p = \vec{E}_p \exp(-iq_0 \sin \theta y), \end{aligned} \quad (6)$$

i.e., refers to a harmonic plane wave propagating in a particular layer p either in the $+z$ ($\text{Im } \tilde{n}_{pz} > 0$) or $-z$ direction ($\text{Im } \tilde{n}_{pz} < 0$).

In the case of plane waves the layer-resolved permittivity $\tilde{\epsilon}^p(\omega)$ is directly related within the Gaussian system of units to the layer-dependent conductivity $\tilde{\sigma}^p(\omega)$ by¹⁵

$$\tilde{\epsilon}^p(\omega) = \mathbf{I} + \frac{4\pi i}{\tilde{\omega}} \tilde{\sigma}^p(\omega), \quad (7)$$

where \mathbf{I} is the 3×3 identity matrix. As the applied computational scheme for the conductivity tensor provides only

contributions of the type $\tilde{\sigma}^{pq}(\omega)$, in order to preserve Eq. (7), the interlayer and intralayer contributions to the permittivity are given by¹⁵

$$\tilde{\epsilon}^{pq}(\omega) = \delta_{pq} \mathbf{I} + \frac{4\pi i}{\tilde{\omega}} \tilde{\sigma}^{pq}(\omega) \quad \text{for } p, q = 1, \dots, N, \quad (8)$$

with δ_{pq} being the Kronecker symbol. Using the linear material equations it was shown that the layer-resolved permittivities $\tilde{\epsilon}^p(\omega)$ can be obtained self-consistently from the contributions $\tilde{\epsilon}^{pq}(\omega)$.¹⁴ Since at least in the case of polar geometry and normal incidence very little differences between the zeroth order for the layer-resolved permittivities,

$$\tilde{\epsilon}^p(\omega) = \sum_{q=1}^N \tilde{\epsilon}^{pq}(\omega) \quad \text{for } p = 1, \dots, N, \quad (9)$$

and their self-consistent counterparts arise,¹⁴ in the following instead of using a self-consistent procedure simply Eqs. (8) and (9) are used.

B. Harmonic plane waves in a layer

By using the Gaussian system of units and suppressing for matters of simplicity the frequency dependence of all quantities, the propagation of a plane wave as given in Eq. (6) for an arbitrary layer p is completely described by the Helmholtz equation¹⁷

$$\sum_{\nu=x,y,z} (\tilde{n}_p^2 \delta_{\mu\nu} - \tilde{n}_{p\mu} \tilde{n}_{p\nu} - \tilde{\epsilon}_{\mu\nu}^p) \mathcal{E}_{p\nu} = 0 \quad (\mu = x, y, z) \quad (10)$$

and the curl Maxwell equation

$$\vec{\mathcal{H}}_p = \vec{n}_p \times \vec{\mathcal{E}}_p. \quad (11)$$

For a given $\tilde{\epsilon}^p$ the normal modes of the electromagnetic wave propagating through layer p —i.e., the nontrivial solutions of Helmholtz equation—are obtained by solving the Fresnel (characteristic) equation associated with Eq. (10), (Ref. 18):

$$|\tilde{n}_p^2 \delta_{\mu\nu} - \tilde{n}_{p\mu} \tilde{n}_{p\nu} - \tilde{\epsilon}_{\mu\nu}^p| = 0 \quad (\mu, \nu = x, y, z). \quad (12)$$

For each normal mode k —namely, $\vec{n}_p^{(k)}$ —the Helmholtz equation (10) then directly provides the components $\vec{\mathcal{E}}_p^{(k)}$ of the electric field, which substituted into Eq. (11) finally yield the magnetic field $\vec{\mathcal{H}}_p^{(k)}$.¹⁹

In the case of $M_p \parallel 0y$, the dielectric tensor for a cubic system is of the form

$$\tilde{\epsilon}^p = \begin{pmatrix} \tilde{\epsilon}_{xx}^p & 0 & \tilde{\epsilon}_{xz}^p \\ 0 & \tilde{\epsilon}_{yy}^p & 0 \\ \tilde{\epsilon}_{zx}^p & 0 & \tilde{\epsilon}_{zz}^p \end{pmatrix}, \quad \text{where } \tilde{\epsilon}_{zz}^p \neq 0. \quad (13)$$

It should be noted that in considering $\tilde{\epsilon}_{zx}^p \neq -\tilde{\epsilon}_{xz}^p$, the symmetry of $\tilde{\epsilon}^p$ is lower than the form to be found in the literature.^{20–22} The reason for this assumption is that in the case of the interlayer contributions $\tilde{\epsilon}^{pq}$ ($p \neq q$) indeed $\tilde{\epsilon}_{zx}^{pq} \neq -\tilde{\epsilon}_{xz}^{pq}$. Therefore is not clear at all from the beginning which symmetry $\tilde{\epsilon}^p$ assumes by summing up all interlayer and intralayer contributions.

For the dielectric tensor $\tilde{\epsilon}^p$ and the complex refraction vector \tilde{n}_p as given by Eqs. (13) and (5), the coefficients of the fourth-order characteristic equation (12),

$$\tilde{n}_{pz}^4 + a\tilde{n}_{pz}^2 + b = 0, \quad (14)$$

are given by

$$a = \left(1 + \frac{\tilde{\epsilon}_{yy}^p}{\tilde{\epsilon}_{zz}^p}\right) \sin^2 \theta + \frac{\tilde{\epsilon}_{xz}^p \tilde{\epsilon}_{zx}^p}{\tilde{\epsilon}_{zz}^p} - \tilde{\epsilon}_{xx}^p - \tilde{\epsilon}_{yy}^p$$

and

$$b = [(\tilde{\epsilon}_{xx}^p - \sin^2 \theta)(\tilde{\epsilon}_{zz}^p - \sin^2 \theta) - \tilde{\epsilon}_{zx}^p \tilde{\epsilon}_{xz}^p] \frac{\tilde{\epsilon}_{yy}^p}{\tilde{\epsilon}_{zz}^p}.$$

Two of the four solutions $\tilde{n}_{pz}^{(k)}$ ($k=1, \dots, 4$) are always situated in the lower half of the complex plane ($\text{Im } \tilde{n}_{pz}^{(k)} < 0$), whereas the other two solutions are in the upper half ($\text{Im } \tilde{n}_{pz}^{(k)} > 0$) of the complex plane. The first type of solutions, denoted in the following by $\tilde{n}_{pz}^{(1)}$ and $\tilde{n}_{pz}^{(2)}$, corresponds to two plane waves propagating downward—i.e., in the $-z$ direction—and the other type $\tilde{n}_{pz}^{(3)}$ and $\tilde{n}_{pz}^{(4)}$ refers to plane waves propagating upward—namely, in the $+z$ direction.

For each solution $\tilde{n}_{pz}^{(k)}$ ($k=1, \dots, 4$) of the characteristic equation (14), the electric field satisfies the Helmholtz equation (10). Because not all of these equations are independent, Eq. (10) can be solved only for two components of the electric field by keeping the third one arbitrary. Following the strategy proposed by Mansuripur in Refs. 19 and 23, one gets all fields as listed from Table I, in which

$$\alpha_p^{(k)} = \begin{cases} \frac{\tilde{\epsilon}_{zx}^p \tilde{n}_{pz}^{(k)} \sin \theta}{[\tilde{n}_{pz}^{(k)}]^2 \tilde{\epsilon}_{zz}^p - \tilde{\epsilon}_{yy}^p (\tilde{\epsilon}_{zz}^p - \sin^2 \theta)}, & \text{for odd } k, \\ \frac{\tilde{\epsilon}_{xz}^p \tilde{n}_{pz}^{(k)} \sin \theta}{\{[\tilde{n}_{pz}^{(k)}]^2 + \sin^2 \theta - \tilde{\epsilon}_{xx}^p\} (\tilde{\epsilon}_{zz}^p - \sin^2 \theta) + \tilde{\epsilon}_{xz}^p \tilde{\epsilon}_{zx}^p}, & \text{for even } k, \end{cases}$$

and

$$\beta_p^{(k)} = \begin{cases} \frac{\tilde{\epsilon}_{zx}^p \{\tilde{\epsilon}_{yy}^p - [\tilde{n}_{pz}^{(k)}]^2\}}{[\tilde{n}_{pz}^{(k)}]^2 \tilde{\epsilon}_{zz}^p - \tilde{\epsilon}_{yy}^p (\tilde{\epsilon}_{zz}^p - \sin^2 \theta)}, & \text{for odd } k, \\ \frac{\tilde{n}_{pz}^{(k)} \{[\tilde{n}_{pz}^{(k)}]^2 + \sin^2 \theta - \tilde{\epsilon}_{xx}^p\} \sin \theta}{\{[\tilde{n}_{pz}^{(k)}]^2 + \sin^2 \theta - \tilde{\epsilon}_{xx}^p\} (\tilde{\epsilon}_{zz}^p - \sin^2 \theta) + \tilde{\epsilon}_{xz}^p \tilde{\epsilon}_{zx}^p}, & \text{for even } k. \end{cases}$$

C. Kerr rotation and ellipticity angles

Because of the continuity of the tangential components of \vec{E} and \vec{H} at the boundary z_p , the reflectivity matrix \mathcal{R}_p , for a particular layer p ,

$$\begin{pmatrix} \mathcal{E}_{px}^{(3)} \\ \mathcal{E}_{py}^{(4)} \end{pmatrix} = \mathcal{R}_p \begin{pmatrix} \mathcal{E}_{px}^{(1)} \\ \mathcal{E}_{py}^{(2)} \end{pmatrix},$$

is obtained in terms of \mathcal{R}_{p-1} by means of the recursion relation^{19,23}

$$\mathcal{R}_p = -(\mathcal{D}_{p-1} \mathcal{A}_p^{34} - \mathcal{B}_p^{34})^{-1} (\mathcal{D}_{p-1} \mathcal{A}_p^{12} - \mathcal{B}_p^{12}), \quad (15)$$

where the 2×2 matrices are defined as

$$\begin{aligned} \mathcal{D}_{p-1} &= (\mathcal{B}_{p-1}^{12} \mathcal{C}_{p-1}^{12} + \mathcal{B}_{p-1}^{34} \mathcal{C}_{p-1}^{34} \mathcal{R}_{p-1}) \\ &\times (\mathcal{A}_{p-1}^{12} \mathcal{C}_{p-1}^{12} + \mathcal{A}_{p-1}^{34} \mathcal{C}_{p-1}^{34} \mathcal{R}_{p-1})^{-1}, \end{aligned} \quad (16)$$

$$\mathcal{A}_p^{k,k+1} = \begin{pmatrix} 1 & \alpha_p^{(k+1)} \\ \alpha_p^{(k)} & 1 \end{pmatrix},$$

$$\mathcal{B}_p^{k,k+1} = \begin{pmatrix} -\beta_p^{(k)} \cos \theta - \tilde{n}_{pz}^{(k)} \alpha_p^{(k)} & -\beta_p^{(k+1)} \cos \theta - \tilde{n}_{pz}^{(k+1)} \\ \tilde{n}_{pz}^{(k)} & \tilde{n}_{pz}^{(k+1)} \alpha_p^{(k+1)} \end{pmatrix}, \quad (17)$$

and by using the lower boundary z_p as reference plane for the four beams propagating in a layer p the propagation matrices $\mathcal{C}_p^{k,k+1}$ are given by

$$\mathcal{C}_p^{k,k+1} = \begin{pmatrix} \exp[+iq_0 \tilde{n}_{pz}^{(k)} d_p] & 0 \\ 0 & \exp[+iq_0 \tilde{n}_{pz}^{(k+1)} d_p] \end{pmatrix},$$

with $d_p = z_{p+1} - z_p > 0$ being the thickness of layer p . Thus one gets the reflectivity matrix of the first layer on the top of the substrate ($p=1$) as

TABLE I. Solution of the Helmholtz and curl Maxwell equations for longitudinal geometry and oblique incidence following Mansuripur's strategy. (Refs. 19 and 23.)

k	1 ($\text{Im } \tilde{n}_{pz}^{(1)} < 0$)	2 ($\text{Im } \tilde{n}_{pz}^{(2)} < 0$)	3 ($\text{Im } \tilde{n}_{pz}^{(3)} > 0$)	4 ($\text{Im } \tilde{n}_{pz}^{(4)} > 0$)
$\mathcal{E}_{px}^{(k)}$	arbitrary	$\alpha_p^{(2)} \mathcal{E}_{py}^{(2)}$	arbitrary	$\alpha_p^{(4)} \mathcal{E}_{py}^{(4)}$
$\mathcal{E}_{py}^{(k)}$	$\alpha_p^{(1)} \mathcal{E}_{px}^{(1)}$	arbitrary	$\alpha_p^{(3)} \mathcal{E}_{px}^{(3)}$	arbitrary
$\mathcal{E}_{pz}^{(k)}$	$\beta_p^{(1)} \mathcal{E}_{px}^{(1)}$	$\beta_p^{(2)} \mathcal{E}_{py}^{(2)}$	$\beta_p^{(3)} \mathcal{E}_{px}^{(3)}$	$\beta_p^{(4)} \mathcal{E}_{py}^{(4)}$
$\mathcal{H}_{px}^{(k)}$	$-\beta_p^{(1)} \sin \theta + \tilde{n}_{pz}^{(1)} \alpha_p^{(1)} \mathcal{E}_{px}^{(1)}$	$-\beta_p^{(2)} \sin \theta + \tilde{n}_{pz}^{(2)} \mathcal{E}_{py}^{(2)}$	$-\beta_p^{(3)} \sin \theta + \tilde{n}_{pz}^{(3)} \alpha_p^{(3)} \mathcal{E}_{px}^{(3)}$	$-\beta_p^{(4)} \sin \theta + \tilde{n}_{pz}^{(4)} \mathcal{E}_{py}^{(4)}$
$\mathcal{H}_{py}^{(k)}$	$\tilde{n}_{pz}^{(1)} \mathcal{E}_{px}^{(1)}$	$\tilde{n}_{pz}^{(2)} \alpha_p^{(2)} \mathcal{E}_{py}^{(2)}$	$\tilde{n}_{pz}^{(3)} \mathcal{E}_{px}^{(3)}$	$\tilde{n}_{pz}^{(4)} \alpha_p^{(4)} \mathcal{E}_{py}^{(4)}$
$\mathcal{H}_{pz}^{(k)}$	$\mathcal{E}_{px}^{(1)} \sin \theta$	$\alpha_p^{(2)} \mathcal{E}_{py}^{(2)} \sin \theta$	$\mathcal{E}_{px}^{(3)} \sin \theta$	$\alpha_p^{(4)} \mathcal{E}_{py}^{(4)} \sin \theta$

$$\mathcal{R}_1 = (\mathcal{D}_0 \mathcal{A}_1^{34} - \mathcal{B}_1^{34})^{-1} (\mathcal{B}_1^{12} - \mathcal{D}_0 \mathcal{A}_1^{12}),$$

if \mathcal{D}_0 for the substrate is known. Because the substrate is a semi-infinite bulk without any boundaries, $\mathcal{R}_0=0$,^{19,23} and therefore Eq. (16) immediately yields

$$\mathcal{D}_0 = \mathcal{B}_0^{12} (\mathcal{A}_0^{12})^{-1},$$

where the 2×2 matrices \mathcal{A}_0^{12} and \mathcal{B}_0^{12} are of form as given in Eq. (17). From the reflectivity matrix \mathcal{R}_1 in Eq. (15), \mathcal{R}_2 *en suite*, and so on, until the reflectivity matrix \mathcal{R}_N of the surface layer is obtained.

The continuity of the tangential components of \vec{E} and \vec{H} at the interface at $z_{N+1}=0$ then yields the surface reflectivity matrix

$$R_{\text{surf}} = -(\mathcal{D}_N - \mathcal{B}_{N+1}^{34})^{-1} (\mathcal{D}_N - \mathcal{B}_{N+1}^{12}) = \begin{pmatrix} \tilde{r}_{xx} & \tilde{r}_{xy} \\ \tilde{r}_{yx} & \tilde{r}_{yy} \end{pmatrix}, \quad (18)$$

where by taking into account that the dielectric tensor in the vacuum is given by $\tilde{\epsilon}_{\mu\nu}^{N+1} = \delta_{\mu\nu}(\mu, \nu=x, y, z)$,

$$\mathcal{B}_{N+1}^{12} = \begin{pmatrix} 0 & \frac{1}{\cos \theta} \\ -\cos \theta & 0 \end{pmatrix}, \quad \mathcal{B}_{N+1}^{34} = \begin{pmatrix} 0 & -\frac{1}{\cos \theta} \\ \cos \theta & 0 \end{pmatrix}.$$

Finally for p -polarized incident light the longitudinal Kerr rotation angle θ_K and Kerr ellipticity angle ϵ_K can be obtained from the complex Kerr angle Φ_K ,^{24,25}

$$\Phi_K = \theta_K + i\epsilon_K \simeq -\frac{\tilde{r}_{xy}}{\tilde{r}_{yy}} \cos \theta, \quad (19)$$

where the complex reflectivity coefficients \tilde{r}_{xy} and \tilde{r}_{yy} follow from Eq. (18).

IV. RESULTS AND DISCUSSIONS

A. Investigated structures

Examining the experimentally determined concentration profiles, one immediately realizes that with the exception of 0.25 ML of Fe mainly two different situations occur: the surface layer contains either both Fe and Pd without forming a perfect stoichiometric binary alloy—e.g., 0.46, 1.50, and 1.97 ML of Fe (see the corresponding entries in the first column of Tables II and III or on top of such a layer there is an additional small amount of Fe like for 0.66, 0.89, 1.10,

TABLE II. Concentration profiles of fcc layered systems Fe/Pd(100) containing fractional numbers of Fe layers as experimentally determined by fitting the x-ray diffraction data (Ref. 3) and the corresponding model profiles used in the calculations. Not listed are the seven (eight) Pd buffer layers to the Pd(100) substrate on the right. Boldface subscripts in the second column mark layers containing nonstoichiometric binary alloys: in the third column they point out differences with respect to the experimental concentration profiles.

Fe (ML)	Experimentally determined concentration profiles ^a fcc Fe/Pd(100)	Model layered system concentration profiles I
0.25	Pd _{0.15} /Fe _{0.25} Pd _{0.75} /	Pd _{0.00} Fe _{0.25} /Pd _{0.75} /
0.46	Fe _{0.25} Pd _{0.18} /Fe _{0.06} Pd _{0.94} /Fe _{0.15} Pd _{0.85} /	Fe _{0.25} Pd _{0.75} /Fe _{0.06} Pd _{0.94} /Fe _{0.15} Pd _{0.85} / ^(a)
0.66	Fe _{0.04} /Fe _{0.37} Pd _{0.25} /Fe _{0.10} Pd _{0.90} /Fe _{0.15} Pd _{0.85} /	Fe _{0.41} Pd _{0.59} /Fe _{0.10} Pd _{0.90} /Fe _{0.15} Pd _{0.85} /
0.89	Fe _{0.03} /Fe _{0.21} Pd _{0.64} /Fe _{0.35} Pd _{0.65} /Fe _{0.30} Pd _{0.70} /	Fe _{0.24} Pd _{0.78} /Fe _{0.35} Pd _{0.65} /Fe _{0.30} Pd _{0.70} /
1.10	Fe _{0.15} /Fe _{0.30} Pd _{0.60} /Fe _{0.40} Pd _{0.60} /Fe _{0.25} Pd _{0.75} /	Fe _{0.45} Pd _{0.55} /Fe _{0.40} Pd _{0.60} /Fe _{0.25} Pd _{0.75} /
1.24	Fe _{0.27} /Fe _{0.26} Pd _{0.74} /Fe _{0.42} Pd _{0.58} /Fe _{0.29} Pd _{0.71} /	Fe _{0.27} Pd _{0.73} /Fe _{0.26} Pd _{0.74} /Fe _{0.42} Pd _{0.58} /Fe _{0.29} Pd _{0.71} /
1.50	Fe _{0.29} Pd _{0.17} /Fe _{0.47} Pd _{0.53} /Fe _{0.27} Pd _{0.73} /Fe _{0.47} Pd _{0.53} /	Fe _{0.29} Pd _{0.71} /Fe _{0.47} Pd _{0.53} /Fe _{0.27} Pd _{0.73} /Fe _{0.47} Pd _{0.53} /
1.97	Fe _{0.64} Pd _{0.29} /Fe _{0.57} Pd _{0.43} /Fe _{0.37} Pd _{0.63} /Fe _{0.39} Pd _{0.61} /	Fe _{0.64} Pd _{0.36} /Fe _{0.57} Pd _{0.43} /Fe _{0.37} Pd _{0.63} /Fe _{0.39} Pd _{0.61} /

^aReference 3.

TABLE III. Concentration profiles of fcc layered systems Fe/Pd(100) containing fractional numbers of Fe layers as experimentally determined by fitting the x-ray diffraction data (Ref. 3) and the corresponding model profiles used in the calculations. Not listed are the seven (eight) Pd buffer layers to the Pd(100) substrate on the right. Boldface subscripts in the second column mark layers containing nonstoichiometric binary alloys: in the third column they point out differences with respect to the experimental concentration profiles. Also listed are theoretical profiles that correspond to an experimental Fe coverage of 0.46, 1.50, and 1.97 ML and in total contain 1.00 (a) and 2.04 (b) ML of Fe, respectively.

Fe (ML)	Experimentally determined concentration profiles ^a fcc Fe/Pd(100)	Model layered system concentration profiles II
0.25	Pd _{0.15} /Fe _{0.25} Pd _{0.75} /	Pd _{0.15} Vac _{0.85} /Fe _{0.25} Pd _{0.75} /
0.46	Fe _{0.25} Pd _{0.18} /Fe _{0.06} Pd _{0.94} /Fe _{0.15} Pd _{0.85} /	Fe _{0.82} Pd _{0.18} /Fe _{0.06} Pd _{0.94} /Fe _{0.12} Pd _{0.88} /(^a)
0.66	Fe _{0.04} /Fe _{0.37} Pd _{0.25} /Fe _{0.10} Pd _{0.90} /Fe _{0.15} Pd _{0.85} /	Fe _{0.04} Pd _{0.96} /Fe _{0.37} Pd _{0.63} /Fe _{0.10} Pd _{0.90} /Fe _{0.15} Pd _{0.85} /
0.89	Fe _{0.03} /Fe _{0.21} Pd _{0.64} /Fe _{0.35} Pd _{0.85} /Fe _{0.30} Pd _{0.70} /	Fe _{0.03} Vac _{0.97} /Fe _{0.21} Pd _{0.79} /Fe _{0.35} Pd _{0.65} /Fe _{0.30} Pd _{0.70} /
1.10	Fe _{0.15} /Fe _{0.30} Pd _{0.60} /Fe _{0.40} Pd _{0.60} /Fe _{0.25} Pd _{0.75} /	Fe _{0.15} Vac _{0.85} /Fe _{0.30} Pd _{0.70} /Fe _{0.40} Pd _{0.60} /Fe _{0.25} Pd _{0.75} /
1.24	Fe _{0.27} /Fe _{0.26} Pd _{0.74} /Fe _{0.42} Pd _{0.58} /Fe _{0.29} Pd _{0.71} /	Fe _{0.27} Vac _{0.73} /Fe _{0.26} Pd _{0.74} /Fe _{0.42} Pd _{0.58} /Fe _{0.29} Pd _{0.71} /
1.50	Fe _{0.29} Pd _{0.17} /Fe _{0.47} Pd _{0.53} /Fe _{0.27} Pd _{0.73} /Fe _{0.47} Pd _{0.53} /	Fe _{0.83} Pd _{0.17} /Fe _{0.47} Pd _{0.53} /Fe _{0.27} Pd _{0.73} /Fe _{0.47} Pd _{0.53} /(^b)
1.97	Fe _{0.64} Pd _{0.29} /Fe _{0.57} Pd _{0.43} /Fe _{0.37} Pd _{0.63} /Fe _{0.39} Pd _{0.61} /	Fe _{0.71} Pd _{0.29} /Fe _{0.57} Pd _{0.43} /Fe _{0.37} Pd _{0.63} /Fe _{0.39} Pd _{0.61} /(^b)

^aReference 3.

and 1.24 ML of Fe. Only for 0.25 ML of Fe the surface layer is partially filled by Pd, since in this case the top layer is formed by a substitutional alloy Pd_xVac_{1-x}, “Vac” denoting empty atomic spheres. It should be noted whenever in Tables II and III reference is made to a composition Fe_xPd_{1-x} the corresponding calculations were performed using the (inhomogeneous) coherent potential approximation; see, e.g., Ref. 26.

One possibility to simulate the experimental structures is to keep the experimental content of Fe unchanged and simply add Pd to form binary alloys of the type Fe_xPd_{1-x}—e.g., in the case of 0.46, 1.50, and 1.97 ML of Fe. In addition, by neglecting the island structure of all surfaces that contain 0.66, 0.89, 1.10, and 1.24 ML of Fe and adding the Fe content of islands on top of the actual surface (in the immediately following layer), a first set of theoretical concentration profiles (I) can be modeled; see Table II. A second set of theoretical concentration profiles (II) is obtained, when allowing Fe to form stoichiometrically perfect layered binary alloys (the cases of 0.46, 1.50, and 1.97 ML of Fe; see Table III). Furthermore, in order to investigate the influence of the islands an attempt is made to simulate this kind of situation by considering a surface of Pd_{0.15}Vac_{0.85} for 0.25 ML of Fe and Fe_xVac_{1-x} for 0.89, 1.10, and 1.24 ML of Fe such that the experimentally determined Fe and Pd content is preserved. To get even more insight into the impact of island formation, in the case of 0.66 ML of Fe the surface layer consists of 0.96 at. % Pd.

Because no other surface x-ray diffraction (SXRD) data are available than those listed in Tables II and III, a series of theoretical structures Fe_N/Pd_{N'}/Pd(100), with $N+N'=0 \bmod 3$ for $N=1, \dots, 10$, has also been considered.

B. Kerr angles

As can be seen from Fig. 1, θ_K shows pronounced maxima between 0.00 and 2.00 ML of Fe, in size compa-

table with the Kerr rotation angle for at least seven (complete) Fe monolayers on top of Pd. This at a first glance (experimentally observed) surprising result,³ in fact, is not totally unexpected, because in a previous paper²⁷ it was already predicted that the Kerr rotation angle can be increased as compared to that of the corresponding ordered system if parts of substrate segregates into the (magnetic) surface. In the case of Co/Pt,²⁷ it was shown that the high polarizability of the paramagnetic substrate leads to a contribution of the (substrate) buffer layers to the optical conductivity larger

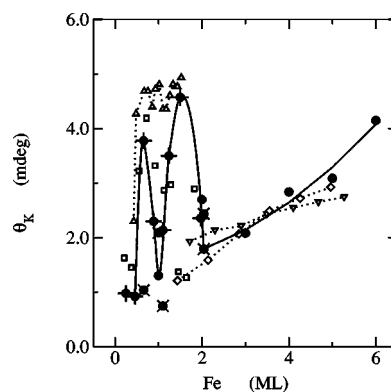


FIG. 1. Longitudinal Kerr rotation angle for oblique incidence ($\theta=70^\circ$) and *p*-polarized light ($\hbar\omega=1.847\ 654$ eV) in the case of fcc Fe/Pd(100). The calculated Kerr rotation angles θ_K in mdeg (10^{-3} deg) corresponding to concentration profiles I (II) are shown as pluses (crosses) and those corresponding to the ordered layered systems Fe_N/Pd(100), with $N \in \mathbb{N}$, as solid circles. The properly scaled experimental Kerr signals (arbitrary units) from Ref. 3 refer to open symbols: squares, up and down triangles denote data from samples obtained by pulse laser deposition performed at temperatures $T=50\text{--}70$ K, while diamonds represent data recorded from thermal deposited probes at room temperature. Dashed lines connect different experimental Kerr signal sets; the solid line follows the regression of the calculated Kerr rotation angles for concentration profiles I and for the ordered layered systems.

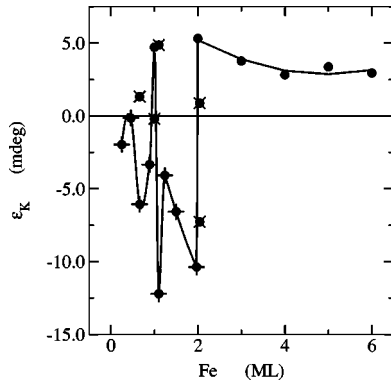


FIG. 2. Longitudinal Kerr ellipticity angle for oblique incidence ($\theta=70^\circ$) and p -polarized light ($\hbar\omega=1.847\ 654$ eV) in the case of fcc Fe/Pd(100). The calculated Kerr ellipticity angles ϵ_K in mdeg (10^{-3} deg) corresponding to concentration profiles I (II) are shown as pluses (crosses) and those corresponding to the ordered layered systems $\text{Fe}_N/\text{Pd}(100)$, with $N \in \mathbb{N}$, as solid circles. The solid line follows the regression of the calculated Kerr ellipticity angles for concentration profiles I and for the ordered layered systems.

than that of the magnetic surface. This is also the case for the system Fe/Pd(100) as easily can be seen by comparing in Fig. 1 the Kerr rotation angles for nominal 1 ML of Fe (see in Table III the entry for Fe 0.46 ML in the column headed by concentration profiles II) with that calculated for the ideal system $\text{Fe}_1/\text{Pd}_5/\text{Pd}(100)$.

From Fig. 1 one immediately can see that the two-peak structure obtained for Fe thicknesses below 2.00 ML agrees well with the experimentally observed pattern, although the calculated minimum around 1.00 ML of Fe is more pronounced than the experimental one. It is well known that only in the polar Kerr effect²⁸ or in a specific transverse configuration^{29,30} does the Kerr angle change linearly with respect to the magnitude of the magnetization. It is therefore not surprising at all that for more than 2 ML of Fe both the calculated and the experimental Kerr rotation angles in Fig. 1 depend quadratically on the number of Fe layers.

The behavior of the Kerr ellipticity angle ϵ_K as a function of the Fe coverage (see Fig. 2) is very similar to that of θ_K in

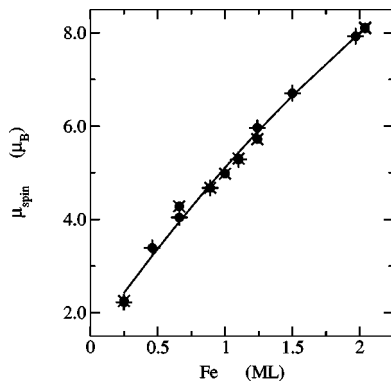


FIG. 3. Spin magnetic moments in the case of fcc Fe/Pd(100). The calculated spin magnetic moments μ_{spin} corresponding to concentration profiles I (II) are shown as pluses (crosses). The solid line follows the regression of the calculated spin magnetic moments for concentration profiles I and II.

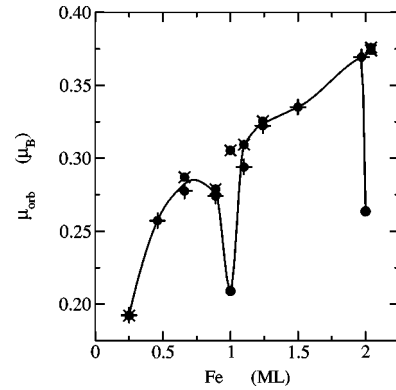


FIG. 4. Orbital magnetic moments in the case of fcc Fe/Pd(100). The calculated orbital magnetic moments μ_{orb} corresponding to concentration profiles I (II) are shown as pluses (crosses) and those corresponding to ordered layered systems $\text{Fe}_{1(2)}/\text{Pd}(100)$ as solid circles. The solid line follows the calculated orbital magnetic moments for concentration profiles I and $\text{Fe}_{1(2)}/\text{Pd}(100)$.

Fig. 1; i.e., several peaks show up for Fe thicknesses below 2.00 ML, whereas above 2.00 ML the Kerr ellipticity angle changes approximately quadratically with the number of Fe monolayers. Unfortunately, since no Kerr ellipticity angles were measured, a comparison of the calculated data with experimental ones cannot be made.

C. Relation to magnetic properties

There seems to be no direct correlation between the longitudinal Kerr rotation angle and the total magnetic moment. As can be seen from Fig. 3, the total spin magnetic moment²⁶ (for all concentration profiles in Tables II and III) is approximately a linear function of the number of Fe layers, extending even to Fe submonolayers. A comparison of the total orbital magnetic moments²⁶ in Fig. 4 with the Kerr rotation angles θ_K in Fig. 1 seems to suggest that the occurrence of

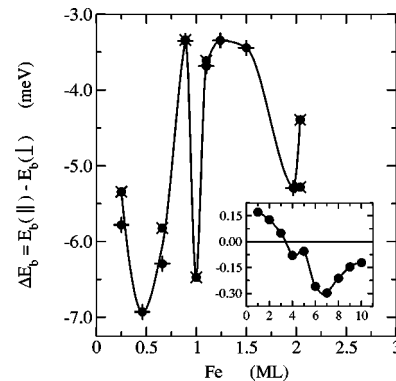


FIG. 5. Band energy contribution to the magnetic anisotropy energy in the case of fcc Fe/Pd(100). The calculated band energy differences ΔE_b corresponding to concentration profiles I (II) are shown as pluses (crosses) and those corresponding to the ordered layered systems $\text{Fe}_N/\text{Pd}(100)$, with $N \in \mathbb{N}$, as solid circles in the inset. The solid lines follow the calculated band energy differences for concentration profiles I (II) and for the ordered layered systems.

peaks for both quantities has to be related to the same intrinsic source. Because the orbital magnetic moment depends linearly on the strength of the spin-orbit coupling, it seems that the sharp maxima of the longitudinal Kerr rotation angle are mainly caused by spin-orbit coupling.

From Fig. 5 one can see that the band energy part of the anisotropy energy (for computational details, see, e.g., Ref. 26) for ideal ordered systems with less than 3 ML Fe favors an out-of-plane magnetization, whereas above 4 ML of Fe the magnetization is always in plane.^{2,4} Since for all systems corresponding to the model concentration profiles I and II, $\Delta E_b < 0$, it can safely be concluded that because of diffusion effects, surface roughness, etc., during the deposition of Fe on top of Pd(100) all these systems have an in-plane magnetization, which in turn cannot be monitored by the polar Kerr effect.

V. SUMMARY

It has been shown that by modeling the Fe/Pd(100) system with submonolayers Fe coverage via concentration profiles appropriate to the experimental ones, the calculated lon-

gitudinal Kerr rotation angles are in very good agreement with the experimental results; i.e., the observed maxima for Fe submonolayer thicknesses and the quadratic dependence on the Fe content above 2 ML of Fe are both well reproduced. It was also found that the longitudinal Kerr rotation angle cannot be simply related to either the (spin or orbital) magnetic moments or to the band energy part of the magnetic anisotropy energy.

ACKNOWLEDGMENTS

We thank Professor H. L. Meyerheim and Dr. J. Barthel for many extremely useful discussions and providing us their experimental SXR and LMOKE data prior to publication. Financial support from the Austrian Science Ministry (Grant No. GZ 45.100), the Austrian Ministry of Economic Affairs and Labour (Grant No. GZ 98.366/10-I/BS3/04), Wissenschaftlich-Technisches Abkommen Austria-Hungary (Grant No. A-3/03), and in particular from the Technical University Vienna is gratefully acknowledged. We also wish to thank the computing center IDRIS at Orsay as part of the calculations was performed using their facilities.

-
- ¹C. Liu and S. D. Bader, *J. Appl. Phys.* **67**, 5758 (1990).
²C. Liu and S. D. Bader, *Phys. Rev. B* **44**, 2205 (1991).
³H. L. Meyerheim, (private communication).
⁴L. Szunyogh, J. Zablouil, A. Vernes, P. Weinberger, B. Újfalussy, and C. Sommers, *Phys. Rev. B* **63**, 184408 (2001).
⁵K. S. Strandburg, D. W. Hall, C. Liu, and S. D. Bader, *Phys. Rev. B* **46**, 10 818 (1992).
⁶X. F. Jin, J. Barthel, J. Shen, S. S. Manoharan, and J. Kirschner, *Phys. Rev. B* **60**, 11 809 (1999).
⁷J. Quinn, Y. S. Li, H. Li, D. Tian, F. Jona, and P. M. Marcus, *Phys. Rev. B* **43**, 3959 (1991).
⁸J. Barthel, (private communication).
⁹A. Vernes, L. Szunyogh, and P. Weinberger, *Phase Transitions* **75**, 167 (2002).
¹⁰J. M. Luttinger, in *Mathematical Methods in Solid State and Superfluid Theory*, edited by R. C. Clark and G. H. Derrick (Oliver and Boyd, Edingburgh, 1967), Chap. 4, p. 157.
¹¹C. S. Wang and J. Callaway, *Phys. Rev. B* **9**, 4897 (1974).
¹²L. Szunyogh and P. Weinberger, *J. Phys.: Condens. Matter* **11**, 10 451 (1999).
¹³A. Vernes, L. Szunyogh, and P. Weinberger, *J. Phys.: Condens. Matter* **13**, 1529 (2001).
¹⁴A. Vernes, L. Szunyogh, and P. Weinberger, *Phys. Rev. B* **65**, 144448 (2002).
¹⁵A. Vernes, L. Szunyogh, and P. Weinberger, *Phys. Rev. B* **66**, 214404 (2002).
¹⁶J. D. Jackson, *Classical electrodynamics* (Wiley, New York, 1975).
¹⁷A. K. Zvezdin and V. A. Kotov, *Modern Magneto-optics and Magneto-optical Materials: Studies in condensed matter physics* (Institute of Physics Publishing, Bristol, 1997).
¹⁸L. D. Landau and E. M. Lifshitz, *Electrodynamics of Continuous Media*, Vol. 8 of *Course of Theoretical Physics* (Butterworth-Heinemann, Oxford, 1999).
¹⁹M. Mansuripur, *The Principles of Magneto-Optical Recording* (Cambridge University Press, Cambridge, England, 1995).
²⁰W. H. Kleiner, *Phys. Rev.* **142**, 318 (1966).
²¹W. H. Kleiner, *Phys. Rev.* **153**, 726 (1967).
²²W. H. Kleiner, *Phys. Rev.* **182**, 705 (1969).
²³M. Mansuripur, *J. Appl. Phys.* **67**, 6466 (1990).
²⁴G. Metzger, P. Pluvinage, and R. Torguet, *Ann. Phys. (Paris)* **10**, 5 (1965).
²⁵J. Zak, E. R. Moog, C. Liu, and S. D. Bader, *Phys. Rev. B* **43**, 6423 (1991).
²⁶P. Weinberger and L. Szunyogh, *Comput. Mater. Sci.* **17**, 414 (2000).
²⁷A. Vernes, L. Szunyogh, and P. Weinberger, *J. Magn. Mater.* **240**, 216 (2002).
²⁸W. Reim and J. Schoenes, in *Magneto-optical Spectroscopy of f-electron Systems*, edited by K. H. J. Buschow and E. P. Wohlfarth (North-Holland, Amsterdam, 1990), Vol. 5, Chap. 2, p. 133.
²⁹P. S. Pershan, *J. Appl. Phys.* **38**, 1482 (1967).
³⁰R. P. Hunt, *J. Appl. Phys.* **38**, 1652 (1967).